ADVANCED FUNCTIONAL MATERIALS
www.afm-journal.de

High-Entropy Liquid Metal Process for Transparent Ultrathin *p*-Type Gallium Oxide

Laetitia Bardet, Ali Zavabeti, Amar Salih, Dawei Zhang, Mohamed Kilani, Mohammad B. Ghasemian, Anton Tadich, Yunlong Sun, Lucy Johnston, Danyang Wang, Jan Seidel, Francois-Marie Allioux, Cuong Ton-That, Jianbo Tang, and Kourosh Kalantar-Zadeh**

The naturally self-limiting oxide formed on the surface of liquid metals can be exfoliated and transferred onto various substrates. This oxide layer with a thickness of a few nanometers is typically highly transparent and can be engineered for applications in large-area optoelectronics. While the incorporation of solvated elements into the interfacial oxide of post-transition metal-based liquid metals is demonstrated for *n*-doping, achieving *p*-doping in such ultrathin oxide layers remains a significant challenge. In this study, the use of dissolved indium (In), platinum (Pt), gold (Au), palladium (Pd), and copper (Cu) in gallium (Ga)-based alloys is investigated to create a high-entropy liquid metal system. This allows the exfoliation of a *p*-doped ultrathin oxide layer, predominantly composed of gallium oxide (Ga_2O_3). The incorporation of these post-transition metals in this high-entropy system results in their atomic dispersion, with Cu exhibiting limited surface presence. The atomically dispersed Pt, Au, and Pd metals scavenge oxygen during exfoliation at moderate temperatures and release them during cooling down, promoting the emergence of trivalent metallic In in Ga oxide layer. This work presents a novel doping strategy at moderate temperatures to achieve *p*-doped liquid-metal-derived ultrathin Ga_2O_3 layers, which maintain high transparency.

1. Introduction

Developing processes for creating new *p*-type transparent metal oxides is a critical step toward advancing transparent electronics. Efforts to obtain post-transition metal oxides, such as gallium (Ga), indium (In), bismuth (Bi), and tin (Sn) oxides, with the desired doping have been made. However, the challenge remains in maintaining the controlled stoichiometry of the dopants required to achieve *p*-type post-transition metal oxides. Typically, the use of highly energetic beams during deposition, combined with post-deposition annealing, alters the desired properties of both the deposited post-transition metal oxide films and the *p*-dopants. In this context, liquid metal processes offer a promising opportunity for more controlled doping of such oxide layers, as dopants migrate from the liquid metal core into the oxide layer. While most liquid metal doping processes have focused on achieving *n*-type doping

L. Bardet, M. Kilani, M. B. Ghasemian, L. Johnston, F.-M. Allioux, J. Tang, K. Kalantar-Zadeh
School of Chemical Engineering
University of New South Wales (UNSW)
Kensington, NSW 2052, Australia
E-mail: jianbo.tang@unsw.edu.au; kourosh.kalantarzadeh@sydney.edu.au

A. Zavabeti
Department of Chemical Engineering
The University of Melbourne
Parkville, VIC 3010, Australia

The ORCID identification number(s) for the author(s) of this article can be found under https://doi.org/10.1002/adfm.202425108

DOI: 10.1002/adfm.202425108

A. Zavabeti
School of Science
Royal Melbourne Institute of Technology (RMIT) University
Melbourne, VIC 3001, Australia

A. Salih, C. Ton-That
School of Mathematical and Physical Sciences
University of Technology Sydney (UTS)
Ultimo, NSW 2007, Australia

D. Zhang, Y. Sun, D. Wang, J. Seidel
School of Materials Science and Engineering
University of New South Wales (UNSW)
Kensington, NSW 2052, Australia

M. B. Ghasemian, F.-M. Allioux, K. Kalantar-Zadeh
School of Chemical and Biomolecular Engineering
University of Sydney
Darlington, NSW 2006, Australia

A. Tadich
Australian Synchrotron, ANSTO
Clayton, VIC 3168, Australia

of post-transition metal oxides,[1,2] reports on controlled doping to create transparent post-transition *p*-type oxides remain limited.[3] In this work, we demonstrate that *p*-type doping of ultrathin post-transition metal oxide films can be effectively achieved using a process based on high-entropy liquid metal alloys (HELMAs).[4]

Surface oxidation is a fundamentally important process of metals and alloys.[5–7] Most metals and alloys naturally form a self-limiting oxide layer in air and the governing kinetics of the emergence of this thin oxide growth are usually interpreted by the Cabrera–Mott model.[5] The surface oxidation of low-melting-temperature liquid metals such as Ga and Ga-based alloys also follows the same model.[8–13] Owing to their liquid state, the parent metals serve as the growth template and substrate for the oxide layer. As the liquid metal is non-polar and in liquid state, the oxide layer and the liquid metal interact weakly with each other, which allows the thin oxide skin to be easily delaminated from the liquid metal surface through facile exfoliation processes.[9] This offers an appealing strategy for the synthesis of highly transparent, large-area, single-layer, or multilayer 2D metal oxides for electronics, optoelectronics, coatings, and sensing applications.[1,3,14–23] Compared to conventional approaches for fabricating 2D or thin-film metal oxides,[24,25] the liquid-metal-enabled method can be performed at room temperature or slightly elevated temperatures, while avoiding the need for complex and costly vacuum processes and equipment. In this regard, Zavabeti et al. showed that the surface composition of the oxide skin of liquid metals depends on the reactivity of the solvated metal relative to that of the liquid metal, which can be predicted by comparing their Gibbs free energy of formation.[9] Since the first demonstration of this method,[26] a variety of 2D metal oxides have been obtained using this method including simple oxides such as gallium oxide (Ga_2O_3),[3,9,17] lead monoxide (PbO),[16] bismuth oxide (Bi_2O_3),[27] tin monoxide (SnO),[26] and more complex binary oxide such as indium tin oxide (ITO)[1] and bismuth-tin oxide.[2] Different exfoliation techniques and post-processing methods have also been applied for modified properties and improved functionalities.[15,19,26,28,29] These progresses, enabled by the liquid-metal-based methods, demonstrate possibilities that are challenging to achieve with pre-existing strategies. However, as previously discussed, the formation of *p*-type 2D metals oxides through liquid metal processes has remained an elusive task.

Liquid metals have the capability to dissolve a range of solute metals at relatively low temperatures.[4,30,31] The surface presence and distribution of these solvated elements depend on the metallic solvent-solute interactions unique to each system. Consequently, the incorporation of these elements into the surface oxide layer during the oxidation process is expected to be system specific. For instance, Ghasemian and co-workers investigated Bi_2O_3-doping of SnO using Sn-based liquid alloys and found substantial property tuning resulting from variations in the constituent ratio[2] and solute elements.[32] Papp and co-workers investigated the incorporation of platinum (Pt) and palladium (Pd) into the Ga_2O_3 in the Pt-Ga and Pd-Ga liquid alloy systems.[33,34] When the Pt-Ga liquid alloy was carefully exposed to low-dose oxygen, Pt is found to be uniformly distributed in the Ga_2O_3 surface layer.[33] By contrast, Pd was not detected in the Ga_2O_3 during oxidation, instead, Pd was located below the oxide layer at the oxide-liquid metal interface.[34] Such observations, lead to question whether it is possible to expand the doping capability to other metals. In addition, experimental parameters such as the oxygen content, the oxidation/exfoliation temperature, the nominal ratio of the solutes, and the entropy of the liquid alloy can have considerable influence on the element doping of the liquid metal surface oxide.[2–4,32–34]

Despite significant progress, many fundamental aspects of surface oxidation in liquid metals and the associated doping of interfacial 2D oxides remain inadequately investigated, as acknowledged by the liquid metal research community.[3,19,28,31,35] To date, studies have mostly focused on liquid alloys with limited number of (one or two) solutes.[2,3,33] The doping of the liquid metal oxides in multi-solute systems, where increased entropy and more complex solvent-solute synergy can exist,[4] is still largely underexplored. Moreover, according to the Cabrera–Mott model, the surface oxidation of liquid metals may experience varying conditions and, consequently, different growth dynamics during the formation of the oxide layer.

Another important aspect that has yet to be explored is the use of trivalent dopants, such as In, for developing *p*-type films. To date, studies have been limited to the formation of indium oxide (In_2O_3), which is a fully stoichiometric oxide of In and is intrinsically considered *n*-type.[36–38] Demonstrating the ability of In to migrate the exfoliated oxide layer without being oxidized is a crucial process that could lead to the formation of *p*-type metal oxides.

In this work, we investigate the multi-element doping of the surface-formed liquid metal oxide layer during the self-limiting oxidation of the eutectic gallium indium (EGaIn) liquid metal containing multiple dilute solvated elements, creating a quasi high-entropy system. We dissolve gold (Au), copper (Cu), Pd, and Pt in the parent EGaIn liquid metal and the Ga-based liquid alloy is referred to as quasi HELMA. The present work is a significant expansion of our previously published work[4] in which HELMA nanodroplets have been investigated. In the past work, our investigation was limited to the bulk properties of HELMA. Here the main goal of our work is to further explore the features of the self-limiting oxide layers of HELMA.

Using the same nominal ratio of 0.5 atomic percentage (at%) of the four elements, we observe temperature-dependent incorporation of In, Pt, Au, and Pd into the exfoliated oxide layer, with varied doping ratios. By stark contrast, Cu remains absent in the surface oxide under all experimental conditions. Ga_2O_3 is intrinsically a *n*-type metal oxide transparent semiconductor known for its wide bandgap (≈4.8 eV). Efforts have been made to create *p*-type Ga_2O_3, which is still challenging.[3,39–41] By comparing the band structures of the exfoliated oxide from EGaIn and the exfoliated oxide from quasi HELMA-EGaIn, we show that our liquid-metal-based doping strategy leads to a transition of Ga_2O_3 from *n*-type to *p*-doped, by allowing the migration of the trivalent In element in metallic state, along with a high optical transmittance (>92% at 400 nm and >95% at 800 nm).

2. Results and Discussion

We start with investigating the doping of the surface-formed metal oxide layer with a thickness of a few nanometers during the self-limiting oxidation of EGaIn liquid metal alloy (**Figure 1a**).

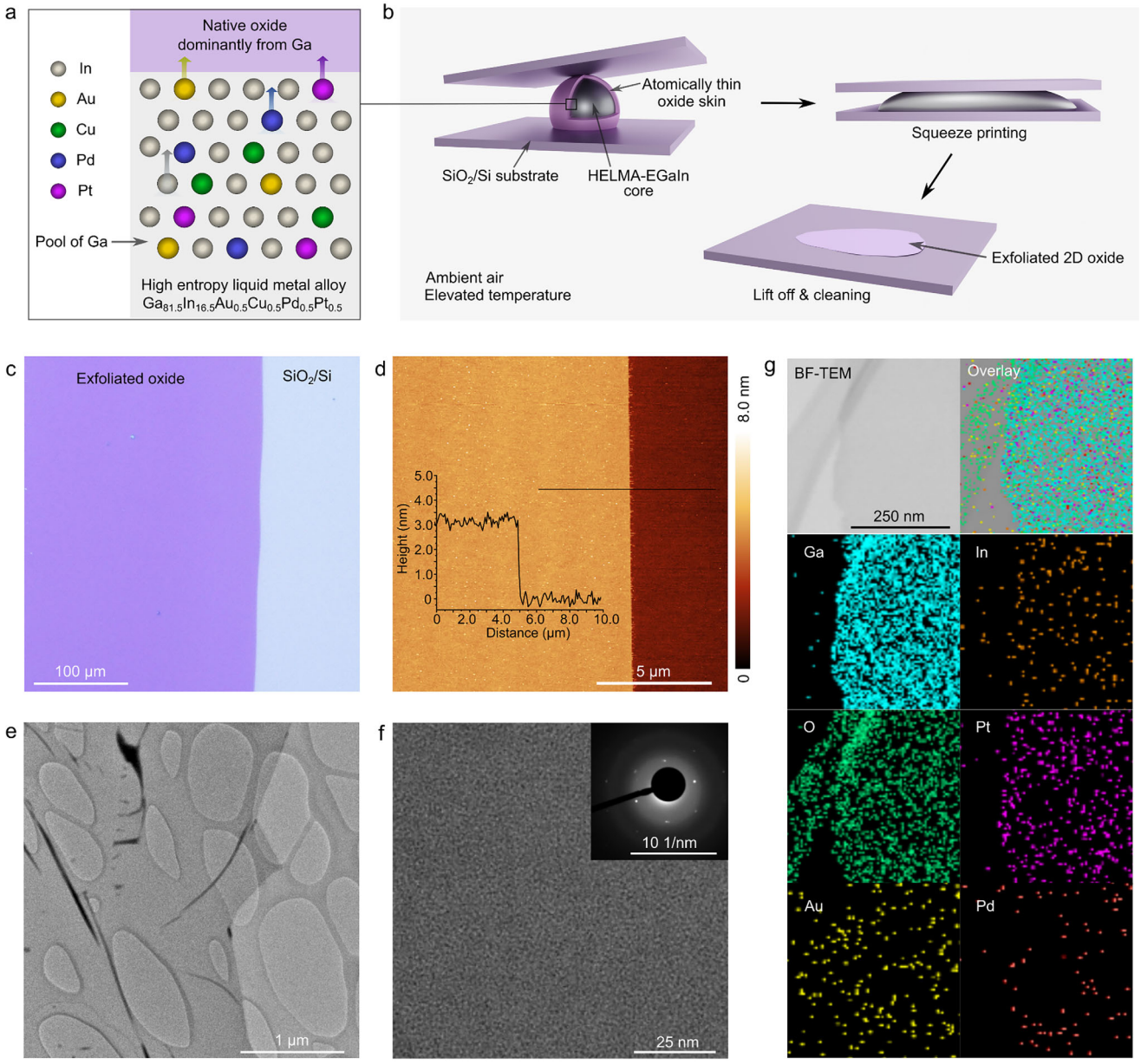

Figure 1. a) Schematic illustration describes the formation of quasi HELMA-EGaIn self-limiting 2D layer and shows the doping possibilities of this oxide layer as a result of elemental migrations of metallic constituents toward it. b) Schematic illustrations of squeeze-printing and exfoliation of 2D oxide sheet. c) Optical image of a 2D oxide sheet exfoliated at 350 °C onto a SiO_2/Si substrate. d) AFM topography image and height profile (along the solid black line) of an exfoliated 2D oxide sheet. e) TEM image of a 2D oxide sheet exfoliated at 350 °C onto a lacey-carbon-coated Cu TEM grid. f) HRTEM image and SAED pattern (inset) showing the structure of the 2D oxide which is mainly amorphous. g) Bright-field TEM image and EDS elemental mapping of Ga, In, O, Pt, Au, and Pd of the 2D oxide sheet. The mapping of Cu is not included as the Cu signal from the TEM grid interferes with the analysis.

The entropy of this system is increased by dissolving multiple elements of Au, Pt, Pd, and Cu.[4] This quasi HELMA-EGaIn (hereafter referred to as HELMA-EGaIn for brevity) has a nominal element atomic ratio of $Ga_{81.5}In_{16.5}Au_{0.5}Cu_{0.5}Pd_{0.5}Pt_{0.5}$, which is designed so that the solute metals remain dissolved in EGaIn under our experimental conditions (Experimental Section).[4] The 2D liquid metal oxide is formed at an elevated temperature of 350 °C, and its exfoliation is achieved by a squeeze-printing technique (Figure 1b, Experimental Section) and then cooled down to room temperature. These exfoliated 2D oxide sheets, typically featuring millimeter lateral dimensions, are transferred onto SiO_2/Si substrates (Figure 1c; Figure S1, Supporting Information). These oxide sheets are free of liquid metal residuals after cleaning (Experimental Section). It is practical to reduce metallic inclusions and wrinkles by introducing automated exfoliation methods and avoid using hands in the exfoliation process. The possibility of using such systems has already been shown by different research groups.[19,42]

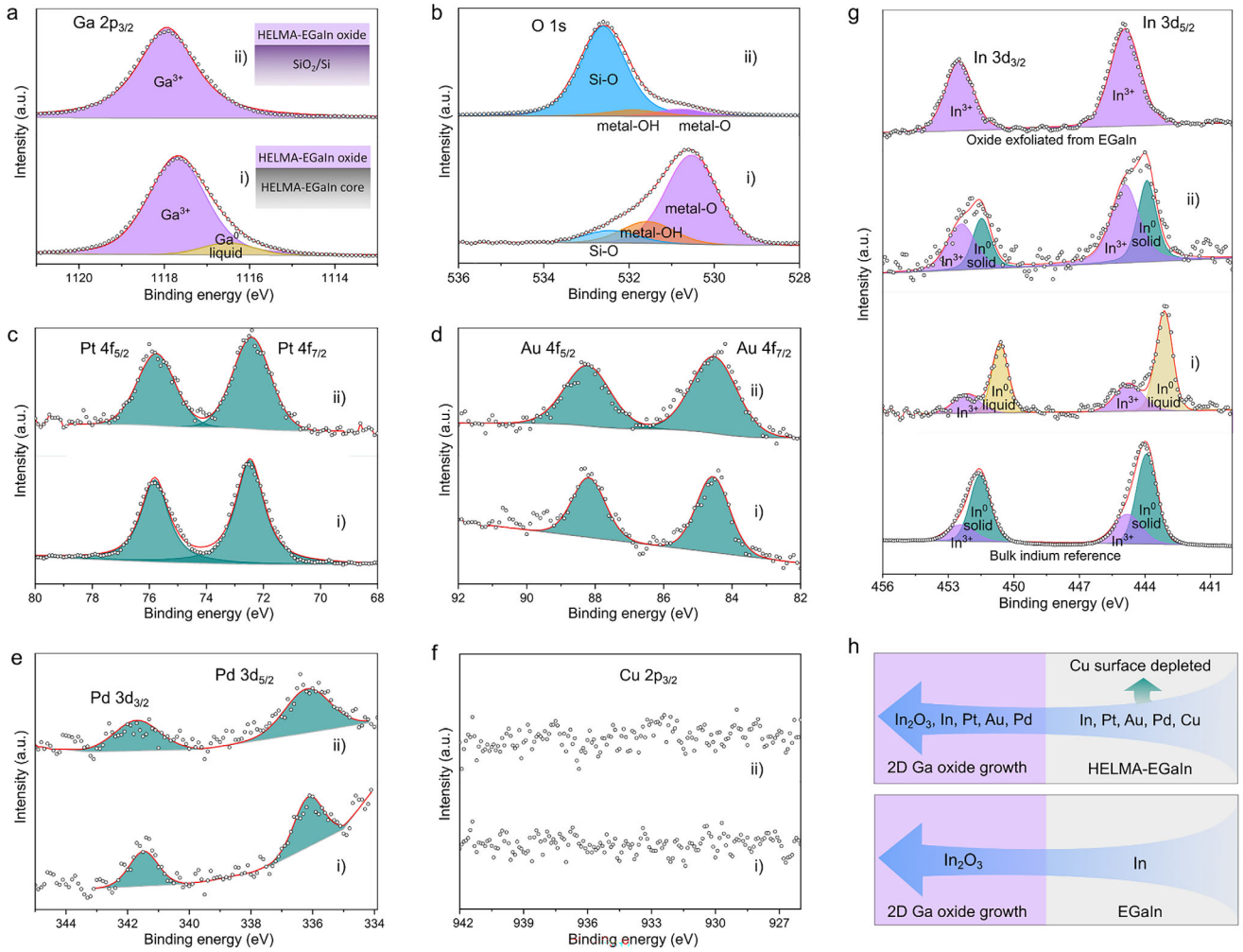

Figure 2. XPS spectra of a) Ga 2p, b) O 1s, c) Pt 4f, d) Au 4f, e) Pd 3d and f) Cu 2p and g) In 3d of i) the surface of the HELMA-EGaIn and ii) the exfoliated oxide sheet of HELMA-EGaIn. For both samples, their oxidation and exfoliation (if performed) took place at 350 °C. For comparison, In 3d spectra of a solidified bulk In sample after heated up to 350 °C and an oxide layer exfoliated at 350 °C from EGaIn are added to g) as references. The XPS characterization is conducted at room temperature. h) Schematic illustrations presenting the compositions of the self-limiting oxide layers of HELMA-EGaIn and EGaIn formed at 350 °C.

Atomic force microscopy (AFM) characterization shows that these 2D oxide sheets have a smooth surface with a root mean square (R_q) of $< 0.3 \pm 0.02$ nm (associated to that of a standard SiO_2/Si substrate underneath) and a thickness of 3.1 ± 0.2 nm (Figure 1d). The AFM topography collected from multiple samples indicates that the self-limiting oxide layer thickness is ≈3 nm (Figure S2, Supporting Information), which matches that of previous reports.[9] While wrinkling and folding occasionally occur in the exfoliated 2D oxide sheets, large-area uniform regions are more frequently seen in the samples (Figures S1 and S2, Supporting Information). Under a transmission electron microscopy (TEM), such wrinkles and folds are observable in ultrathin oxide sheets exfoliated onto TEM grids (Figure 1e), together with liquid metal residues as TEM samples are not cleaned (Experimental Section).

High-resolution TEM (HRTEM) images and selected area electron diffraction (SAED) patterns both show that the 2D oxide formed on the surface of HELMA-EGaIn are mostly amorphous with occasional crystalline regions which might be due to long exposure of the beam and/or liquid metal residues (Figure 1f). TEM-based energy-dispersive X-ray spectroscopy (EDS) analysis reveals the predominance of Ga and O in the 2D oxide (Figure 1g; Figure S3, Supporting Information). The other elements, including the dopants In, Pt, Au, and to a much lesser extent Pd, show a uniform lateral distribution across the oxide sheets. We note that the presence and distribution of Cu are not included in the EDS analysis due to the interference from the Cu-containing TEM grid.

X-ray photoelectron spectroscopy (XPS) was performed at room temperature to analyze the chemical state and the ratio of constituent elements in exfoliated oxide sheets (SiO_2/Si substrate-supported) of HELMA-EGaIn (**Figure 2**). All the constituent elements of the samples are detected in the XPS spectra from both i) the surface of HELMA-EGaIn and ii) the exfoliated oxide at 350 °C of HELMA-EGaIn (Figure 2a–e,g), except for Cu (Figure 2f). Since the oxide layer is a few nanometers

thick, XPS can reach the surface of the liquid metal underneath the oxide. However, Cu is not detected in the case where the oxide layer is supported by the HELMA-EGaIn. Notably, the deeper Cu presence in the HELMA-EGaIn sample is confirmed by scanning electron microscopy-energy dispersive X-ray analysis (SEM-EDX) which has a detection depth larger than XPS (Figure S4, Supporting Information). These measurements suggest that the Cu exists considerably far away from the surface of the HELMA-EGaIn, suggesting possible Cu nucleation inside the bulk, far from the surface of HELMA-EGaIn. The main goal of adding Cu within the liquid metal alloy was to increase the intrinsic molar entropy of the EGaIn solvent.[4] Theoretical calculations (Figure S5, Supporting Information) show that the molar entropy of HELMA-EGaIn at room temperature is slightly higher than that of the EGaIn-AuPdPt liquid metal alloy. We have demonstrated that this enhanced entropy in HELMA-EGaIn is achieved by adding Cu, which leads to the atomic dispersion of Pt atoms within the liquid metal matrix rather than promoting the formation of Pt clusters.[4] When Cu is introduced in the HELMA, Pt is atomically dispersed in the Ga oxide layer, as also evidenced by Figure 2c. However, due to the surface Cu depletion effect, Cu did not reach the surface and, consequently, cannot be incorporated into the oxide layer during the oxidation of the HELMA-EGaIn. It is worth noting that Cu inclusion within Ga_2O_3 layer has already been demonstrated when the exfoliation was carried out from a lesser entropy quaternary Ga-In-Sn-Cu alloy.[3]

The Ga 2p XPS spectrum of the oxide layer formed on the HELMA-EGaIn shows both the oxidized state and metallic state of the Ga component (Figure 2a). No metallic Ga peak is observed in the XPS spectra of the exfoliated oxide sheet, which validates that, after cleaning, the oxide layer is free of Ga liquid metal residues. The exfoliated oxide is exclusively composed of Ga_2O_3 (Ga 2p peak at 1117.9 eV). Compared to the XPS spectra collected from the surface of the HELMA-EGaIn (non-exfoliated sample), the Ga 2p peak of the exfoliated oxide from HELMA-EGaIn shows a binding energy shift of +0.3 eV. The O 1s XPS peak at 530.6 eV is assigned to the Ga—O and In—O bonds (Figure 2b) and the high O 1s peak at 532.7 eV corresponds to Si—O bonds from the SiO_2/Si substrate.

The Pt 4f, Au 4f, and Pd 3d peaks of the non-exfoliated samples have contributions from the metallic Pt, Au and Pd dissolved in the liquid metal (graphs i) of Figure 2c–e, respectively). No additional feature, such as broadening or splitting of the peaks, is observed that also suggests Pt, Au, and Pd in the core liquid metal and the exfoliated oxide share a similar metallic state. Thus, Pt, Au and Pd dopants are all assigned to their metallic states when incorporated into the oxide layer. It is very important to note that the binding energies of both Pt 4f and Pd 3d show shifts to higher binding energies (Pt $4f_{7/2}$ at 72.5 eV and Pd $3d_{5/2}$ at 336.2 eV) when compared to standard solid Pt (Pt $4f_{7/2}$ at 71.2 eV) and Pd (Pd $3d_{5/2}$ at 335 eV). These positive peak shifts are attributed to the energy requirements of atomically dispersed Pt and Pd surrounded by less electronegative Ga atoms, as reported in previous studies.[33,43] This observation provides critical evidence for the atomic dispersion of Pt, Au and Pd despite their tendency to cluster with Ga according to their individual phase diagrams upon cooling. The atomic dispersion is attributed to the high-entropy nature of the Ga-based alloy, which arises from mixing multiple metal elements.

Indium XPS spectra of the exfoliated and the surface of HELMA-EGaIn are depicted in Figure 2g. For comparison, we show In 3d XPS spectra of a bulk In sample heated up to 350 °C and cooled down (bottom graph in Figure 2g), and an exfoliated oxide from EGaIn (upper graph in Figure 2g).

As can be seen, In element is mostly metallic for the bulk In pattern, while some In^{3+} content is also observed. On the other side, In element in the exfoliated sheet from EGaIn is dominantly In^{3+}, indicating that In is fully oxidized for this sample. Very interestingly, the oxidation state of In in i) the surface of HELMA-EGaIn and ii) the exfoliated sheet from HELMA-EGaIn are quite different. The In 3d peak of the HELMA-EGaIn surface reveals a significantly higher presence of metallic In compared to In^{3+}, illustrated by a large peak intensity originating from metallic In within the core of the liquid metal alloy. Surprisingly, in contrast to the exfoliated oxide layer from the EGaIn, the In 3d peak intensity in the exfoliated oxide layer from the HELMA-EGaIn still exhibits a strong metallic In component, comparable to that of In^{3+}. These results suggest that the use of HELMA-EGaIn helps in preserving the metallic nature of the In that diffuses into the exfoliated sheet (schematically shown in Figure 1a). The following discussion reveals the likely reason.

It is known that if In metal, with its trivalent nature, is added to a semiconductor, *p*-doping is induced due to the tendency of In to accept electrons.[41] Inversely, if In_2O_3, which is an intrinsically *n*-type semiconductor, is combined with another *n*-type oxide semiconductor (in our case, Ga oxide), the resulting material exhibits a collective *n*-type property.[44] Here, the presence of metallic In in the HELMA-EGaIn exfoliated oxide sheet may lead to the production of a *p*-type layer.

The emergence of metallic In can be explained via the presence of Pt, and Au, and to a lesser extent Pd, during the exfoliation process at 350 °C. It is known that at the elevated temperature of higher than 300 °C, Pt, Au and Pd, which have been previously shown to be atomically dispersed in $Ga_{81.5}In_{16.5}Au_{0.5}Cu_{0.5}Pd_{0.5}Pt_{0.5}$,[4] act as "oxygen scavengers" by adsorbing O atoms from the environment, giving much less chance for In oxide to be formed. Interestingly, Pt, Au and Pd can release the O atoms to the surrounding environment during cooling to room temperature, while at these lower temperatures In has little tendency to oxidize.[45,46] So, the presence of Pt, Au and Pd, promote the formation of metallic In rather than In oxide through the liquid metal exfoliation process at 350 °C.

To complete these XPS observations, the concentration of the constituent elements in the exfoliated 2D oxide is assessed based on quantitative XPS analyses (**Table 1**). Ga is the predominant metal element in its oxidized form while a few percent of In coexists for oxide sheets exfoliated at 350 °C from both EGaIn and HELMA-EGaIn. The favorable formation of Ga oxide over In oxide is mainly governed by the energetics of the metals rather than their relative abundance.[9]

We note that the ratios of Ga and In in the exfoliated Ga oxide layer are overall consistent for both samples. The dopant ratio, including In, Pt, Au, and Pd (no Cu), is only a few percent for the oxide sheet exfoliated from HELMA-EGaIn and the ratio of individual dopants varies considerably (Table 1). The doping ratio of Pt is 1.3 at%, which is about five times higher than that of Au and Pd. Both exfoliated oxide layers show In as the highest doping ratio (≈2.2 at%). As discussed previously (Figure 2g),

Table 1. Quantitative XPS analysis of element concentration of the oxide sheet of HELMA-EGaIn and EGaIn prepared at 350 °C.

Exfoliated oxide from	Atomic concentration (at%)[a]							
	Ga	O	In		Pt	Au	Pd	Cu
			Ox.	Met.				
HELMA-EGaIn[b]	48.3 ± 2.6	47.6 ± 2.7	1.2 ± 0.4	1.0 ± 0.3	1.3 ± 0.3	0.3 ± 0.1	0.3 ± 0.2	0.0
EGaIn[c]	51.2 ± 3.3	46.3 ± 3.2	2.5 ± 0.2	0.0	–	–	–	–

[a] The values and standard errors represent the average composition for four different measured samples exfoliated at 350 °C. The corresponding XPS data can be found in Figures S6 and S7 (Supporting Information); [b] Nominal ratio of the parent liquid metal: $Ga_{81.5}In_{16.5}Au_{0.5}Cu_{0.5}Pd_{0.5}Pt_{0.5}$; [c] Nominal ratio of the parent liquid metal: $Ga_{83.2}In_{16.8}$.

unlike the exfoliated sheet from the surface of EGaIn, the exfoliated sheet from HELMA-EGaIn interface has a high concentration of In in metallic state (≈1.0 at%). Figure 2h illustrates the oxidation states of the constituents in the limiting oxide layers of both HELMA-EGaIn and EGaIn, formed and exfoliated at 350 °C. The full discussion about the phenomena behind this illustration have been provided in the text.

Further investigation are conducted to assess the effect of the exfoliation temperature. The exfoliation from a much cooler temperature (25 °C) of the HELMA-EGaIn leads also to an oxide sheet which is mainly composed of Ga_2O_3, without metallic Ga residues (**Figure 3**a,b). It is important to note that obtaining an exfoliated oxide from HELMA-EGaIn without liquid metal residues proved significantly more challenging at 25 °C compared to elevated temperatures. XPS spectra of Au 4f and In 3d are comprehensively discussed for further comparison here (Figure 3c,d, respectively).

We note that the Au 4f peaks of the exfoliated oxide at 25 °C show a binding energy shift of +0.7 eV compared to the Au 4f peaks of the oxide exfoliated at 350 °C (Figure 3c). This result can be associated with the atomic dispersion of Au elements in films exfoliated at 350 °C and likely Au clustering within exfoliated sheet at room temperature. The oxidation state of In is also quite different for both exfoliated samples. While In has a very strong metal component for the 350 °C-exfoliated sample (Figures 3d and 2g), it only shows to emerge as In^{3+} when the exfoliation process is performed at 25 °C (Figure 3d). This observation further highlights the critical accessibility of highly dispersed Pt, Au and Pd elements at 350 °C, which scavenge oxygen from In and prevent its complete oxidation.

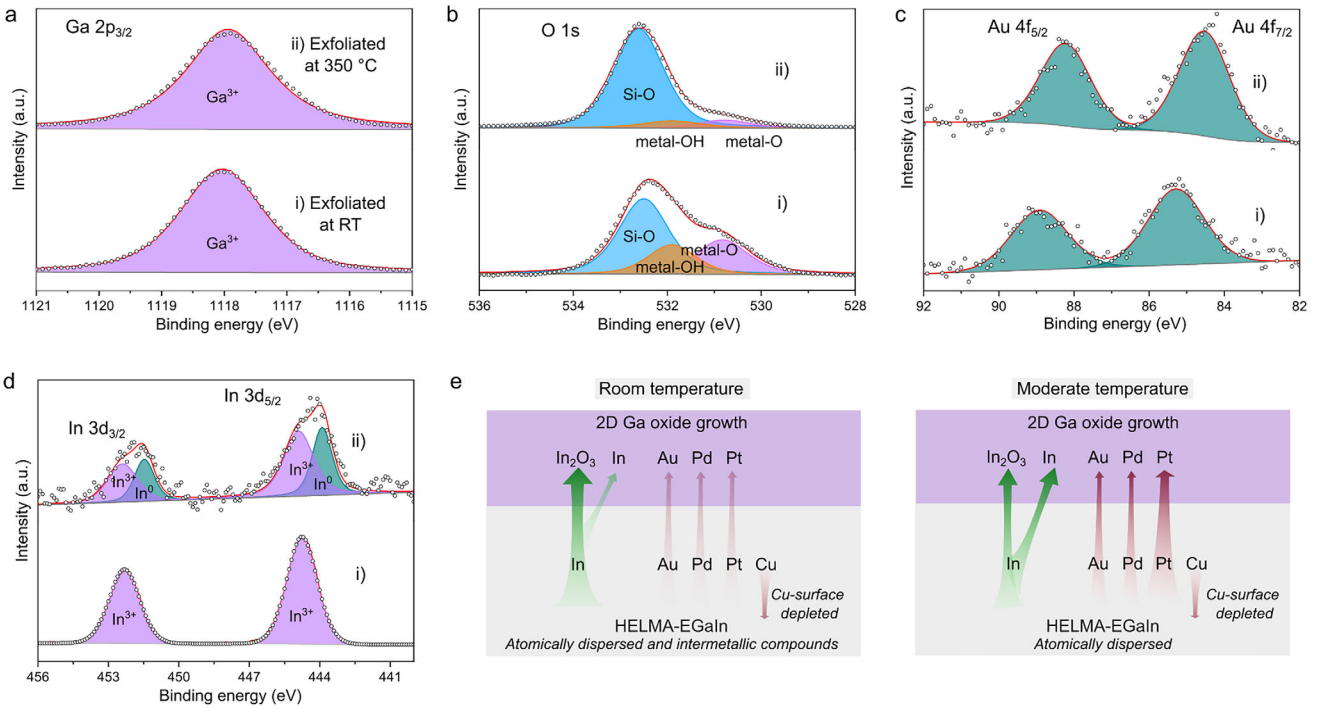

Figure 3. XPS spectra of a) Ga 2p, b) O 1s, c) Au 4f, and d) In 3d of the exfoliated oxide sheet of HELMA-EGaIn exfoliated at i) room temperature (RT, upper graphs) and ii) 350 °C (bottom graphs). The XPS characterization is conducted at room temperature. e) Schematic illustration of the changes in the dispersion and oxidation states of metals occurring at temperatures of 25 and 350 °C, penetrating from the bulk of alloy to the 2D oxide layer.

Table 2. Quantitative XPS analysis of element concentration of the oxide sheet of HELMA-EGaIn prepared at two exfoliation temperatures of 25 and 350 °C.

Exfoliated oxide from	Atomic concentration (at%)[a]							
	Ga	O	In		Pt	Au	Pd	Cu
			Ox.	Met.				
25 °C	45.9 ± 3.3	47.6 ± 3.2	5.8 ± 4.5	0.3 ± 0.4	0.1 ± 0.1	0.2 ± 0.1	0.1 ± 0.1	0.0
350 °C [b]	48.3 ± 2.6	47.6 ± 2.7	1.2 ± 0.4	1.0 ± 0.3	1.3 ± 0.3	0.3 ± 0.1	0.3 ± 0.2	0.0

[a] The values and standard errors represent the average composition for four different measured samples exfoliated at 25 °C and 350 °C of the parent liquid metal: $Ga_{81.5}In_{16.5}Au_{0.5}Cu_{0.5}Pd_{0.5}Pt_{0.5}$; [b] The values and standard errors correspond to the one shown in Table 1.

The atomic ratio of elements in the oxide layer at 25 °C differs from that at elevated temperatures (**Table 2**), mainly due to intermetallic compounds present at room temperature. We previously showed via differential scanning calorimetry (DSC) analysis, that no intermetallic compounds exist above 300 °C in HELMA-EGaIn due to increased entropy.[4] Above 300 °C, the absence of these compounds enables the diffusion of atomically dispersed Au, Pt, and Pd through the oxide layer of HELMA-EGaIn. The changes in the incorporation, dispersion, and oxidation state of metals at both exfoliation temperatures are summarized in Figure 3e.

These results highlight that the doping of In, Pt, Au and Pd in the exfoliated oxide is temperature-sensitive and that their doping ratio is related to the nature of each element. This further shows that these two major-component solvent metals behave differently from that of the minor solute metals in terms of their temperature dependence and changes in chemical state when forming the surface oxide. The presence of Pt, Au, and Pd metals within the oxide sheet may lead to a *n*-type behavior of the oxide sheet. However, In metal, present in the oxide layer in a ratio comparable to the sum of Pt, Au, and Pd ratios, competes with these metal dopants to lead to an oxide layer with a *p*-type behavior.

In order to prove the *p*-type nature of the exfoliated film from HELMA-EGaIn sample, further characterizations were conducted. Compared to the oxide layer exfoliated at 350 °C from EGaIn (control sample), the incorporation of In, Pt, Au, and Pd dopants within the exfoliated oxide sheet induces a small decrease of the optical transmittance in the 400–800 nm range (**Figure 4a**). Nevertheless, the exfoliated oxide from HELMA-EGaIn remains highly transparent in the visible region (>92% at 400 nm and >95% at 800 nm). Electron energy loss spectroscopy (EELS) shows that the bandgap (E_g) is equal to 4.3 and 3.5 eV for the control sample and the exfoliated oxide from HELMA-EGaIn, respectively (Figure 4b). The shrinkage of the bandgap occurs typical when dopants of sufficiently high concentrations are introduced into a semiconductor.

Note that the EELS spectra were collected from the oxide sheet exfoliated onto TEM grids, for which the post-exfoliation washing step to remove residual liquid metal could not be successfully performed without damaging the grids. Consequently, a peak originating from the surface plasmon resonance of the residual liquid metal nanodroplets appears ≈6.5 eV of the EELS spectra.[47] The work functions (WFs) were obtained using ultraviolet photoelectron spectroscopy (UPS). Subtracting 10 V from the secondary electron cutoff (the intercept of UPS curves on the *x*-axis, Figure 4c) to account for the sample bias gives the WF values. The WF increases from 3.5 eV for the control sample (EGaIn) to 3.9 eV for the HELMA-EGaIn sample. The separation between the Fermi level and the valence band maximum (VBM) is determined from the XPS valence band spectra (Figure 4d). It is found that the Fermi level-VBM separation decreased significantly from 3 to 0.5 eV for the control sample and the exfoliated oxide from HELMA-EGaIn, respectively, due to the doping effect.

The results from EELS, UPS and XPS characterization allow us to plot the electronic band structures of both samples. Ga_2O_3 is normally *n*-type.[39,40] The same is true for the control sample that has a minor In oxide component, as indicated by the close energy levels between its Fermi level and conduction band minimum (CBM) (Figure 4e). The energy gap between the Fermi level and VBM is considerably larger in comparison between the two samples. For the oxide sheet exfoliated from HELMA-EGaIn, the Fermi level and VBM become very close (Fermi level-VBM energy gap of 0.5 eV), implying a *p*-type band structure (Figure 4f). These results can be compared with the XPS valence band spectra of oxide sheets exfoliated at 350 °C from a liquid Ga and a liquid $Ga_{98}Au_{0.5}Cu_{0.5}Pd_{0.5}Pt_{0.5}$ alloy and are shown in Figure S8 (Supporting Information). This further confirms that the observed *p*-type behavior of the oxide sheet exfoliated from HELMA-EGaIn arises from the presence of metallic In. In addition, the response to NO_2 (an oxidizing gas) of the exfoliated oxide from HELMA-EGaIn of the films is obtained to further confirms the *p*-type characteristic of HELMA-EGaIn (Figure S9, Supporting Information). These results demonstrate the effectiveness of our liquid metal-based method in achieving controlled *p*-type and *n*-type doping of the exfoliated layer.

The 2D oxide sheets were exfoliated on ITO transparent substrates for conductive AFM (c-AFM) measurements. ITO substrates provide excellent electrical conductivity as well as desirable affinity for the surface oxide of the liquid metals, enabling successful exfoliation. ITO substrate was selected because of its work function of ≈4.3 eV,[48] which closely matches the VBM energy of the HELMA-EGaIn oxide layer. In the c-AFM measurement configuration, the current passes through a conductive Pt-coated AFM tip, the 2D oxide sheet, and the ITO substrate under an applied voltage (inset of Figure 4g,h). Topography and current maps for both exfoliated oxide sheets are depicted in Figure S10 (Supporting Information). When a voltage bias from −1 to +1 V is applied, no detectable current signal is measured for the control sample (Figure 4g), which is expected for wide bandgap

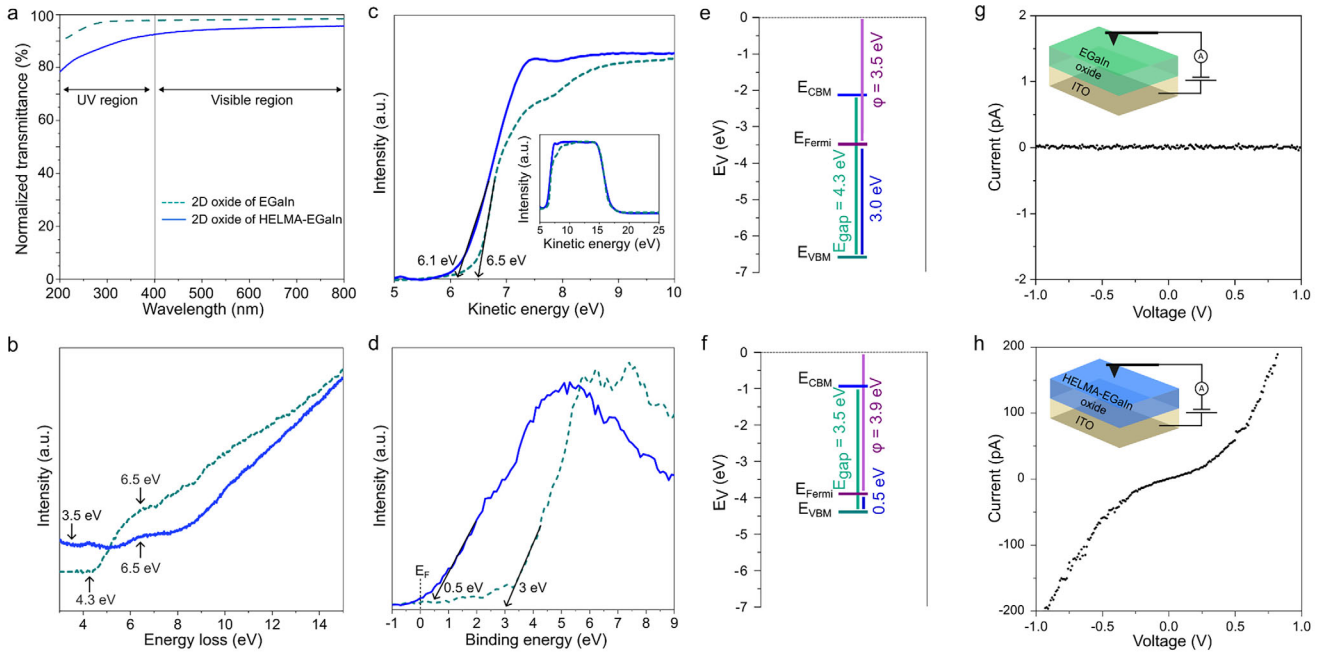

Figure 4. a) Normalized transmittance in the UV-visible region of the exfoliated oxide sheets of EGaIn (control sample) and HELMA-EGaIn. b) EELS spectra of the oxide sheets for both samples. The bandgap value and the location of the plasmonic peak (originating from metallic nanodroplet inclusion) are marked. c) UPS spectra of the 2D oxide sheets. The black arrows are linear fits to the secondary electron cutoff with *x*-intercept at 6.5 and 6.1 eV for the control sample and the exfoliated oxide from HELMA-EGaIn, respectively. d) XPS valence bands. e,f) Energy band diagram constructed based on the UPS, XPS, and EELS data. g,h) *I–V* curves of the control sample (g) and the exfoliated oxide from HELMA-EGaIn (h), both on an ITO substrate, measured by c-AFM.

semiconductor predominantly composed of Ga_2O_3. By contrast, a near-linear *I–V* curve is measured for the HELMA-EGaIn exfoliated sheet under the same bias voltage range (Figure 4h). The *I–V* curve of the exfoliated oxide from HELMA-EGaIn indicates a back-to-back Schottky diode behavior usually seen in metal/semiconductor/metal configuration.[49] The block region of the *I–V* curve is narrow (knee point at ≈0.3 V), indicating a narrow depletion layer width and strong doping. We use the Hertz model[50] to estimate the effective contact area between the tip apex and the 2D oxide sheet, which allows us to calculate the electrical resistivity of the 2D HELMA-EGaIn exfoliated oxide sheet (Note S1, Supporting Information). The electrical resistivity of this 2D oxide sheet is found to be ≈30 Ω•m, suggesting a *p*-doped layer by the metal In element. To show another example of the viability of the process and the exfoliated 2D HELMA-EGaIn oxide layers for developing junction-based devices, we also exfoliated 2D HELMA-EGaIn oxide onto $La_{0.7}Sr_{0.3}MnO_3$ (LSMO) layer interfaced with a $SrTiO_3$ (LSMO/STO) substrate. LSMO/STO is highly conductive as it supports high mobility 2D electron at its interface. The discussion and IV curve are presented in Figure S11 (Supporting Information). These results confirm that our method effectively dopes the oxide layer, converting *n*-type to *p*-type without post-annealing or external infusion doping techniques.

3. Conclusion

In summary, we explored the selective doping of a Ga_2O_3 layer with a thickness of a few nanometers by dopants including In, Au, Pt, and Pd using a liquid metal process that took advantage of high-entropy alloys. The ultrathin oxide was formed by the self-limiting oxidation of Ga-based liquid metals and the doping took place during oxidation at moderate temperature. The oxide sheet was transferred by exfoliation of the self-limiting surface oxide of liquid metal alloy onto substrates to characterize the chemical states, structure, and electrical and optical properties. We investigated the incorporation of various dopants, including 0.5 at% Pt, Au, Pd, and Cu, along with the presence of a eutectic In component, in the oxide layers at different temperatures. The solute metals gave rise to distinct temperature-dependent doping behaviors as a result of the system-specific solvent-solute interactions and energetics, rather than their relative abundance. In this process, Pt, Au, and Pd played a crucial role in scavenging and releasing O from the environment, allowing the formation of trivalent metallic In. Indium-dominant doping, achieved through the high-entropy system, induced *p*-type doping of the ultrathin Ga_2O_3 layer, resulting in enhanced electrical conductivity and yet a high optical transmittance. In brief, the presence of metallic elements reduces the optical transmittance and the bandgap size of exfoliated 2D HELMA-EGaIn oxide layer in comparison to 2D EGaIn oxide layer. In the meantime, the introduction of trivalent In made 2D HELMA-EGaIn oxide layer *p*-type in comparison to 2D EGaIn oxide layer, which is *n*-type.

Our work offers fundamental insights into the solvent-solute interactions in multi-component high-entropy liquid metal systems for creating highly transparent *p*-type semiconducting oxides, which are essential for establishing *pn* junctions for LED/OLEDs devices and solar cells.

4. Experimental Section

Materials: The procedure of the preparation of the liquid metal alloy in this work was based on a previous work.[4] The precursors metals, Ga and In beads (purity of 99.999%, Indium Corporation) were first alloyed at the eutectic ratio (Ga:In = 75:25 by weight percentage) in a glass vial on a hotplate at 500 °C for 4h. Solute elements, Au, Pt, Pd, and Cu in the form of short wires (purity ≥ 99.99% for all the metals, Sigma–Aldrich), were thermally dissolved at the same concentrations (0.5 at% each) into the EGaIn metallic solvent at 500 °C for 4 h to increase the mixing entropy and provide a homogeneously mixed $Ga_{81.5}In_{16.5}Au_{0.5}Cu_{0.5}Pd_{0.5}Pt_{0.5}$ liquid metal,[4] avoiding the formation of any intermetallic compounds with Ga.

Different types of substrates were used for the exfoliation of 2D liquid metal oxide layer: namely, SiO_2/Si substrate with a SiO_2 thickness of 280 nm (University Wafer), *p*-type Si substrate (University Wafer), quartz substrate (University Wafer), ITO substrate (University Wafer), and LSMO/STO substrates. Here, LSMO thin films were grown on (001) STO single-crystal substrates (a = 0.3905 nm, cubic) by Laser Molecular Beam Epitaxy (LMBE, PASCAL Combi, Japan).[51] A KrF excimer laser (λ = 248 nm) with an energy density of 2.5 J cm^{-2}, temperature of 800 °C, oxygen partial pressure of 200 mTorr, and frequency of 5 Hz were adopted for the deposition. The substrates were successively sonicated in acetone and ethanol for 10 min at 20 °C, washed with deionized water, and dried using N_2 gas. Then they were subjected to 2 min of air plasma (Tergeo) at 75 W under a low vacuum (400 mTorr). Before the printing process, substrates were cut into centimeter-scale squares.

Fabrication of Exfoliated 2D Oxide Sheets by Squeeze Printing: The procedure of the printing process used in this work is based on a previous work.[1] During the printing process, a liquid droplet of the metal alloy was deposited onto a substrate using a glass Pasteur pipette. The substrate and droplet were both heated at 350 °C which is above the melting point of all the alloys. One minute after depositing the droplet onto the substrate, another substrate, preheated at 350 °C, was pressed manually onto the center of the droplet to squeeze it between the two substrates. Then the top substrate was lifted in the vertical direction. This technique leads to the exfoliation of homogeneous ultrathin oxide sheets onto both substrates in ambient air. The delamination of the liquid metal oxide skin occurs thanks to strong van der Waals interactions with the substrate. Both substrates have exfoliated 2D oxide sheets and can be used. After this squeeze-printing step, some metal residues remain on the exfoliated sheets. They can be easily removed using standard cleaning methods based on previous works.[1,3,16] The mechanical cleaning methods have been proved to be efficient, since the exfoliated layers after cleaning have been used for making devices such as capacitive touch screen or in homojunction diodes. In the present work, after squeeze-printing, the exfoliated oxide layers with liquid metal residues on the surface were immersed in a beaker filled with ethanol (not water, to avoid further oxidation of the oxide) and then heated at 100 °C. In specific rare cases, in which liquid metal residues were observed, the surface of the exfoliated oxide layers was gently wiped off with a soft lint-free cotton swab, with minimal applied pressure to avoid damaging the surface. The cleaning procedure was repeated until no liquid metal residues (i.e., bright shiny dots) were observed by optical microscope. Large area samples, of mm lateral dimensions, were produced as shown in Figure 1c and Figure S1c (Supporting Information).

Characterizations: AFM was used for measuring the thickness and surface topography of the 2D oxide sheets, and the measurement was performed on a Bruker Dimension Icon AFM using Scanasyst-air AFM tips. Image processing was performed using Gwyddion software. c-AFM was conducted on an AIST-NT Smart SPM 1000 under room temperature in ambient conditions. Pt-coated tips (Mikromasch HQ: NSC35/Pt, radius <30 nm) were used for the c-AFM measurements with different DC biases applied to the probe. 2D liquid metal oxide samples exfoliated on the ITO were tested. The substrates were placed onto a metallic disc, and silver paste was deposited on the edge of the oxide layers to form electrical contact between the oxide layer and the disc. The test circuit was formed by the AFM probe, the oxide layer and the conductive substrate layer (Figure 4g,h). A JEOL JEM-F200 TEM with a cold field emission gun (FEG) operating at 200 kV was employed for high-resolution imaging, collecting energy-dispersive EDS maps, and conducting EELS. The 2D oxide sheet was directly deposited on lacey TEM Cu grids for these measurements. EDS and EELS mappings were performed using a Gatan GIF Continuum-S spectrometer. The EELS measurements were conducted in STEM mode. EELS maps were collected with a resolution of 2 nm/pixel, using 20 accumulations and an exposure time of 1 ms/pixel, while a channel dispersion of 0.015 eV/Ch was selected. The emission current was reduced to 5 µA during the EELS measurements, achieving a zero-loss peak's full width at half maximum (ZLP-FWHM) of 0.4 eV. The spectroscopy data and maps were processed using Gatan DigitalMicrograph software suit (v3.5). EDS-SEM were performed on a JEOL JSM-IT500 system (accelerating voltage). Optical microscopy images of the 2D oxide sheets on SiO_2/Si substrates were captured using an Olympus optical microscope (BX53MTRF-S). The optical transmittance in standard transmission UV/VIS mode of the 2D oxide sheets (exfoliated on quartz substrates) were measured using a PerkinElmer UV/VIS lambda 365 spectrophotometer from 250 to 800 nm with a step of 1 nm. A bare quartz substrate was recorded for comparison. The surface chemistry and valence band of the exfoliated oxide sheets on SiO_2/Si substrates were analyzed by XPS at room temperature using a Thermo Scientific K-alpha XPS spectrometer (ESCALAB250Xi) equipped with a mono-chromated Al Kα source ($h\nu$ = 1486.68 eV). The pass energy of the analyzer for the region scans was set to 20 eV. UPS of the secondary cutoff using He(I) emission line ($h\nu$ = 21.2 eV) from a helium gas discharge lamp and the CHA was performed to acquire the work functions (WF) of the samples. A sample bias of −10 V was applied during UPS measurements. Samples were directly exfoliated on *p*-type Si substrate. The work function was calculated by subtracting the sample bias from the energy cutoff. For the gas sensing characterization, silver paste (ProSciTech) was used as electrical contact and the exfoliated oxide samples were exposed to three 5-min cycles of 10 ppm nitrogen dioxide gas (balanced with nitrogen), separated by nitrogen purges, in a LINKAM gas chamber. A total flow rate of 500 sccm was maintained using mass flow controllers. The samples were connected to a Wayne Kerr 6500B Impedance Analyzer to continuously monitor their electrical impedance during exposure. Gas flow control and data acquisition were automated using LabVIEW software. The chamber temperature was maintained at 200 °C using a LINKAM temperature control system.

Supporting Information

Supporting Information is available from the Wiley Online Library or from the author.

Acknowledgements

This work was supported by the Australian Research Council (ARC) Discovery Early Career Researcher Award (DE220100816 and DE240100743), ARC Discovery Project (DP240101086), ARC Centre of Excellence FLEET (CE170100039), ARC Laureate Fellowship grant (FL180100053). The authors thank the Surface Analysis Laboratory at the Mark Wainwright Analytical Centre at UNSW Sydney, and Sydney Analytical at the University of Sydney.

Open access publishing facilitated by University of New South Wales, as part of the Wiley - University of New South Wales agreement via the Council of Australian University Librarians.

Conflict of Interest

The authors declare no conflict of interest.

Author Contributions

The conceptualization of the study was carried out by L.B., J.T., and K.K.-Z. Data curation was performed by L.B., A.Z., A.S., D.Z., and M.B.G. The

methodology was developed by L.B., A.Z., A.S., D.Z., M.K., M.B.G., F.-M.A., C.T.-T., J.T., and K.K.-Z. The investigation was conducted by L.B., A.Z., A.S., D.Z., M.K., M.B.G., A.T., Y.S., and L.J. Formal analysis was undertaken by L.B., A.Z., A.S., M.B.G., D.W., J.S., F.-M.A., C.T.-T., J.T., and K.K.-Z. Funding acquisition was handled by F.-M.A., J.T., and K.K.-Z., while supervision was provided by J.T. and K.K.-Z. The original draft was written by L.B., J.T., and K.K.-Z. All authors contributed to the review and revision of the manuscript.

Data Availability Statement

The data that support the findings of this study are available from the corresponding author upon reasonable request.

Keywords

2D metal oxide, Cabrera–Mott oxidation, doping, gallium oxide, liquid metal

Received: December 18, 2024
Revised: February 11, 2025
Published online:

[1] R. S. Datta, N. Syed, A. Zavabeti, A. Jannat, M. Mohiuddin, M. Rokunuzzaman, B. Y. Zhang, M. A. Rahman, P. Atkin, K. A. Messalea, M. B. Ghasemian, E. D. Gaspera, S. Bhattacharyya, M. S. Fuhrer, S. P. Russo, C. F. McConville, D. Esrafilzadeh, K. Kalantar-Zadeh, T. Daeneke, *Nat. Electron.* **2020**, *3*, 51.
[2] M. B. Ghasemian, A. Zavabeti, M. Mousavi, B. J. Murdoch, A. J. Christofferson, N. Meftahi, J. Tang, J. Han, R. Jalili, F.-M. Allioux, M. Mayyas, Z. Chen, A. Elbourne, C. F. McConville, S. P. Russo, S. Ringer, K. Kalantar-Zadeh, *Adv. Mater.* **2021**, *33*, 2104793.
[3] Q. Li, B.-D. Du, J.-Y. Gao, J. Liu, *Appl. Phys. Rev.* **2023**, *10*, 011402.
[4] F.-M. Allioux, S. Nazari, M. B. Ghasemian, A. Zavabeti, Z. Pei, J. Leverett, S. Rafiezadeh, A. K. Salih, C. P. Irvine, M. Baharfar, L. Bardet, M. S. Widjajana, Y. Chi, D. Esrafilzadeh, A. R. Jalili, N. Haghdadi, J. Tang, K. J. Laws, C. Ton-That, T. Daeneke, R. Daiyan, M. A. Rahim, K. Kalantar-Zadeh, *Small Struct.* **2024**, *5*, 2400294.
[5] N. Cabrera, N. F. Mott, *Rep. Prog. Phys.* **1949**, *12*, 163.
[6] A. T. Fromhold, E. L. Cook, *Phys. Rev.* **1967**, *163*, 650.
[7] L. P. Ramírez, F. Bournel, J.-J. Gallet, L. Dudy, F. Rochet, *J. Phys. Chem. C* **2022**, *126*, 2517.
[8] D. Wang, X. Wang, W. Rao, *Acc. Mater. Res.* **1093**, *2021*, 2.
[9] A. Zavabeti, J. Z. Ou, B. J. Carey, N. Syed, R. Orrell-Trigg, E. L. H. Mayes, C. Xu, O. Kavehei, A. P. O'Mullane, R. B. Kaner, K. Kalantar-zadeh, T. Daeneke, *Science* **2017**, *358*, 332.
[10] J.-H. Kim, S. Kim, M. D. Dickey, J.-H. So, H.-J. Koo, *Nanoscale Horiz.* **2024**, *9*, 1099.
[11] W. Jung, M. H. Vong, K. Kwon, J. U. Kim, S. J. Kwon, T. Kim, M. D. Dickey, *Adv. Mater.* **2024**, *36*, 2406783.
[12] J. Liao, C. Majidi, *Adv. Sci.* **2022**, *9*, 2201963.
[13] J. Liao, C. Majidi, *Soft Matter* **2021**, *17*, 1921.
[14] C. K. Nguyen, P. D. Taylor, A. Zavabeti, H. Alluhaybi, S. Almalki, X. Guo, M. Irfan, M. A. Kobaisi, S. J. Ippolito, M. J. S. Spencer, S. Balendhran, A. Roberts, T. Daeneke, K. B. Crozier, Y. Sabri, N. Syed, *Adv. Funct. Mater.* **2024**, *34*, 2309342.
[15] Y. Ye, A. B. Hamlin, J. E. Huddy, M. S. Rahman, W. J. Scheideler, *Adv. Funct. Mater.* **2022**, *32*, 2204235.
[16] M. B. Ghasemian, A. Zavabeti, R. Abbasi, P. V. Kumar, N. Syed, Y. Yao, J. Tang, Y. Wang, A. Elbourne, J. Han, M. Mousavi, T. Daeneke, K. Kalantar-Zadeh, *J. Mater. Chem. A* **2020**, *8*, 19434.
[17] Y. Xu, J. Zhang, X. Han, X. Wang, C. Ye, W. Mu, Z. Jia, K. Qian, *ACS Appl. Mater. Interfaces* **2023**, *15*, 25831.
[18] W. J. Scheideler, K. Nomura, *Adv. Funct. Mater.* **2024**, *34*, 2403619.
[19] M. Kong, M. H. Vong, M. Kwak, I. Lim, Y. Lee, S. Lee, I. You, O. Awartani, J. Kwon, T. J. Shin, U. Jeong, M. D. Dickey, *Science* **2024**, *385*, 731.
[20] A. Goff, P. Aukarasereenont, C. K. Nguyen, R. Grant, N. Syed, A. Zavabeti, A. Elbourne, T. Daeneke, *Dalton Trans.* **2021**, *50*, 7513.
[21] M. Zhang, J. Gong, H. Chang, X. Sun, P. Zhang, J. Fu, L. Liu, X. Li, Y. Wang, W. Rao, *Adv. Funct. Mater.* **2023**, *33*, 2215050.
[22] Y. Wang, S. Wang, H. Chang, W. Rao, *Adv. Mater. Interfaces* **2020**, *7*, 2000626.
[23] J. Lin, Q. Li, T.-Y. Liu, Y. Cui, H. Zheng, J. Liu, *Phys. Status Solidi RRL – Rapid Res. Lett.* **2019**, *13*, 1900271.
[24] B. Konkena, C. Kalapu, H. Kaur, A. Holzinger, H. Geaney, V. Nicolosi, M. D. Scanlon, J. N. Coleman, *ACS Appl. Mater. Interfaces* **2023**, *15*, 58320.
[25] B. Konkena, H. Kaur, R. Tian, C. Gabbett, M. McCrystall, D. V. Horvath, K. Synnatschke, A. Roy, R. Smith, V. Nicolosi, M. D. Scanlon, J. N. Coleman, *Small* **2022**, *18*, 2203918.
[26] B. J. Carey, J. Z. Ou, R. M. Clark, K. J. Berean, A. Zavabeti, A. S. R. Chesman, S. P. Russo, D. W. M. Lau, Z.-Q. Xu, Q. Bao, O. Kavehei, B. C. Gibson, M. D. Dickey, R. B. Kaner, T. Daeneke, K. Kalantar-Zadeh, *Nat. Commun.* **2017**, *8*, 14482.
[27] K. A. Messalea, B. J. Carey, A. Jannat, N. Syed, M. Mohiuddin, B. Y. Zhang, A. Zavabeti, T. Ahmed, N. Mahmood, E. Della Gaspera, K. Khoshmanesh, K. Kalantar-Zadeh, T. Daeneke, *Nanoscale* **2018**, *10*, 15615.
[28] T. Daeneke, K. Khoshmanesh, N. Mahmood, I. A. De Castro, D. Esrafilzadeh, S. J. Barrow, M. D. Dickey, K. Kalantar-zadeh, *Chem. Soc. Rev.* **2018**, *47*, 4073.
[29] J. Ma, F. Krisnadi, M. H. Vong, M. Kong, O. M. Awartani, M. D. Dickey, *Adv. Mater.* **2023**, *35*, 2205196.
[30] K. Kalantar-Zadeh, J. Tang, T. Daeneke, A. P. O'Mullane, L. A. Stewart, J. Liu, C. Majidi, R. S. Ruoff, P. S. Weiss, M. D. Dickey, *ACS Nano* **2019**, *13*, 7388.
[31] K. Kalantar-Zadeh, T. Daeneke, J. Tang, *Science* **2024**, *385*, 372.
[32] M. B. Ghasemian, A. Zavabeti, F.-M. Allioux, P. Sharma, M. Mousavi, M. A. Rahim, R. Khayyam Nekouei, J. Tang, A. J. Christofferson, N. Meftahi, S. Rafiezadeh, S. Cheong, P. Koshy, R. D. Tilley, C. F. McConville, S. P. Russo, C. Ton-That, J. Seidel, K. Kalantar-Zadeh, *Small* **2024**, *20*, 2309924.
[33] M. Grabau, S. Krick Calderón, F. Rietzler, I. Niedermaier, N. Taccardi, P. Wasserscheid, F. Maier, H.-P. Steinrück, C. Papp, *Surf. Sci.* **2016**, *651*, 16.
[34] H. Wittkämper, S. Maisel, M. Moritz, M. Grabau, A. Görling, H.-P. Steinrück, C. Papp, *Phys. Chem. Chem. Phys.* **2021**, *23*, 16324.
[35] A. Martin, C. Du, B. Chang, M. Thuo, *Chem. Mater.* **2020**, *32*, 9045.
[36] C. K. Nguyen, A. Mazumder, E. L. Mayes, V. Krishnamurthi, A. Zavabeti, B. J. Murdoch, X. Guo, P. Aukarasereenont, A. Dubey, A. Jannat, X. Wei, V. K. Truong, L. Bao, A. Roberts, C. F. McConville, S. Walia, N. Syed, T. Daeneke, *Adv. Mater. Interfaces* **2023**, *10*, 2202036.
[37] C. K. Nguyen, M. X. Low, A. Zavabeti, B. J. Murdoch, X. Guo, P. Aukarasereenont, A. Mazumder, A. Dubey, A. Jannat, M. A. Rahman, K. Chiang, V. K. Truong, L. Bao, C. F. McConville, S. Walia, T. Daeneke, N. Syed, *Adv. Opt. Mater.* **2022**, *10*, 2200925.
[38] C. K. Nguyen, M. X. Low, A. Zavabeti, A. Jannat, B. J. Murdoch, E. Della Gaspera, R. Orrell-Trigg, S. Walia, A. Elbourne, V. K. Truong, C. F. McConville, N. Syed, T. Daeneke, *J. Mater. Chem. C* **2021**, *9*, 11815.
[39] S. J. Pearton, J. Yang, P. H. Cary, F. Ren, J. Kim, M. J. Tadjer, M. A. Mastro, *Appl. Phys. Rev.* **2018**, *5*, 011301.
[40] J. Zhang, J. Shi, D.-C. Qi, L. Chen, K. H. L. Zhang, *APL Mater.* **2020**, *8*, 020906.

[41] J. Ma, J. Lin, J. Liu, F. Li, Y. Liu, G. Yang, *Chem. Phys. Lett.* **2020**, *746*, 137308.
[42] Y. Wang, M. Mayyas, J. Yang, J. Tang, M. B. Ghasemian, J. Han, A. Elbourne, T. Daeneke, R. B. Kaner, K. Kalantar-Zadeh, *Adv. Funct. Mater.* **2021**, *31*, 2005866.
[43] M. A. Rahim, J. Tang, A. J. Christofferson, P. V. Kumar, N. Meftahi, F. Centurion, Z. Cao, J. Tang, M. Baharfar, M. Mayyas, F.-M. Allioux, P. Koshy, T. Daeneke, C. F. McConville, R. B. Kaner, S. P. Russo, K. Kalantar-Zadeh, *Nat. Chem.* **2022**, *14*, 935.
[44] O. Bierwagen, *Semicond. Sci. Technol.* **2015**, *30*, 024001.
[45] Z. M. Detweiler, S. M. Wulfsberg, M. G. Frith, A. B. Bocarsly, S. L. Bernasek, *Surf. Sci.* **2016**, *648*, 188.
[46] I. N. Reddy, C. Venkata Reddy, M. Cho, J. Shim, D. Kim, *Mater. Res. Express* **2017**, *4*, 086406.
[47] S.-Y. Tang, D. R. G. Mitchell, Q. Zhao, D. Yuan, G. Yun, Y. Zhang, R. Qiao, Y. Lin, M. D. Dickey, W. Li, *Matter* **2019**, *1*, 192.
[48] R. Schlaf, H. Murata, Z. H. Kafafi, *J. Electron Spectrosc. Relat. Phenom.* **2001**, *120*, 149.
[49] A. J. Chiquito, C. A. Amorim, O. M. Berengue, L. S. Araujo, E. P. Bernardo, E. R. Leite, *J. Phys. Condens. Matter* **2012**, *24*, 225303.
[50] H. Hertz, *Misc. Pap.*, Mcmillan and Co, New York, **1896**, 146–162.
[51] Y. Sun, L. Zhang, Q. Huang, Z. Chen, D. Wang, M. M. Seyfouri, S. L. Y. Chang, Y. Wang, Q. Zhang, X. Liao, S. Li, S. Zhang, D. Wang, *Adv. Sci.* **2022**, *9*, 2203926.